Predictive Assembly of Nanowire Arrays using Floating Electrode Dielectrophoresis

BY

NEHAL ARYAAN
B.E., OSMANIA UNIVERSITY, HYDERABAD, INDIA, 2016

THESIS

Submitted as partial fulfillment of the requirements
for the degree of Master of Science in Mechanical Engineering
in the Graduate College of the
University of Illinois at Chicago, 2018

Chicago, Illinois

Defense Committee:

Arunkumar Subramanian, Chair and Advisor
Jeremiah Abiade
Amit Ranjan Trivedi, Electrical and Computer Engineering

ACKNOWLEDGMENTS

TABLE OF CONTENTS

LIST OF FIGURES

LIST OF FIGURES (continued)

LIST OF ABBREVIATIONS

NWs	Nanowires
MEMS	Microelectromechanical Systems
NEMS	Nanoelectromechanical Systems
CNTs	Carbon Nanotubes
DEP	Dielectrophoresis
TEM	Transmission Electron Microscopy
FE-DEP	Floating Electrode Dielectrophoresis
C-DEP	Conventional Dielectrophoresis
3-D	Three Dimensional
AC	Alternating Current
FEM	Finite Element Model
FEA	Finite Element Analysis
Si_3N_4	Silicon Nitride
EBL	Electron Beam Lithography
α -MnO$_2$	Alpha Phase-Manganese dioxide
SiO_2	Silicon Di-oxide
V	Voltage

nm   Nanometer

μm   Micrometer

ROI   Region of Influence

SUMMARY

Functional device integration using dielectrophoretic nanoassembly presents important opportunities in diverse applications ranging from nanoelectronics to sensors and energy nanosystems. In recent studies, floating electrode dielectrophoresis has demonstrated alignment precision, directional deposition and relatively better control during the nanoassembly process as compared to conventional dielectrophoresis. This thesis focuses on a 3-D electrokinetic model for predictive assembly of nanowires using floating electrode dielectrophoresis.

A study of the nanowire (NW) trajectories and their localization sites on electrodes, which result from floating electrode dielectrophoresis, was carried out using the COMSOL and MATLAB platforms. Three-dimensional finite element models were produced using the COMSOL software, to calculate the electric field distribution generated by an array of electrode pairs on silicon chips. Results acquired after the analysis were imported to a MATLAB environment, in order to predict the dielectrophoretic forces and trajectories followed by NWs towards eventual deposition on electrodes.

Moreover, the effect of DEP parameters such as deposition time, biasing voltage and NW size on the deposition process (in terms of NW trajectory, assembly position and orientation) was investigated. The accuracy of the finite element models was validated through direct quantitative comparison with the experimental results. The presented modeling approach and its analysis has the potential to enable predictive and scalable assembly of nanomaterials into functional nanodevices.

1   INTRODUCTION AND BACKGROUND

Owing to their excellent mechanical and electrical properties, one-dimensional nanomaterials, such as nanowires, nanotubes and nanobelts have attracted widespread attention. Over the past decade, the focus on these materials has evolved from studies of their intrinsic properties to development of devices for applications such as nanoelectronics [1-5], energy storage [6-8], sensors [9-11], and fuel cells [12-13]. Nanoscale devices are usually built by one of two approaches: top-down and bottom-up methodologies. Top-down techniques utilize direct manipulation of the components or substrates to construct devices, and bottom-up techniques involve aspects of self- or directed-assembly such that the components of a device assume energetically favorable configurations.

A current obstacle to realizing the predicted applications of nanomaterials, such as nanotubes (NTs) and nanowires (NWs), lies in their manipulation and integration into nanodevices like nanoelectromechanical systems (NEMS) and microelectromechanical systems (MEMS). Several assembly methods have been used in the past and these include optical alignment [14], fluidic alignment [15-16], dielectrophoresis (DEP) [5, 9, 17-18], chemically selective deposition [19] and atomic force microscopy based manipulation [20]. Among these nanoassembly methods, dielectrophoretic assembly has the following advantages:

1. Ability to manipulate a variety of nanomaterials, which range from metals to semiconductors and ceramics, as long as they are more polarizable than the suspension medium,

2. Precise manipulation of nanomaterials and simple implementation on silicon chips,

3. Shorter deposition times,

4. Deposition yield of nanomaterials on top of conductive pads or electrodes, which is a preferred location for testing and investigation in most technological applications, and

5. Use of simple equipment without the need for complex control electronics and environmental chambers.

Thus, DEP has been widely utilized in batch fabrication of nanodevices and has demonstrated potential for assembly of nanomaterials with accuracy in terms of both, position and orientation. Past reports on DEP-based nanoassembly include assembly of energy storage devices [6-8], field-effect transistors [13] and gas/chemical/pressure sensors [9-11]. Considerable efforts have been made to optimize DEP assembly and new techniques such as floating-electrode dielectrophoresis (FE-DEP) [which is explained in a later part of this thesis] have created avenues for higher control over manipulation of nano-objects. To control the manipulation of individual nanomaterials and increase the dielectrophoretic deposition yield, understanding the behavior and interaction of different underlying physical forces is essential and this forms the primary focus of this thesis.

1.1 <u>Electrokinetics</u>

Electrokinetics refers to the movement of charged or polarizable objects under the application of an electric field. Thus, electrokinetic forces provide a method for controlled manipulation of particles under the influence of an inhomogeneous electric field. Using techniques based on these forces, positive separation and analysis of various particles such as cells, bacteria and viruses have been demonstrated [21-22]. Furthermore, reference [23] clearly highlights the benefits of electrokinetics through the following statement: "The electrokinetic methodologies are unique in particle manipulation, since they are based on inherent charge distributions within the manipulated materials, their scaling laws are highly compatible with microfluidic systems, and their instrumentation is relatively simple to assemble." Electrophoresis and DEP are two variants of electrokinetic manipulation techniques. Electrophoresis refers to the action of electric fields on charged particles. DEP, on the other hand, refers to the manipulation of polarizable particles (with a zero net charge), which are suspended in a liquid medium, through the use of a nonuniform electric field [17, 24-25].

1.2 <u>Dielectrophoresis</u>

DEP is a phenomenon where a force is exerted on a polarizable object, when it is subjected to a non-uniform electric field within a fluidic medium [7, 24-25]. When the particle is more polarizable than the medium in which it is suspended, the DEP force directs the suspended particle towards the region of field maxima. This phenomenon was first discovered by Pohl in 1951. The strength of this DEP force is dependent on the frequency of the applied electric field, shape and size of the nanomaterial, and the electrical properties of the suspension medium and the nanomaterial.
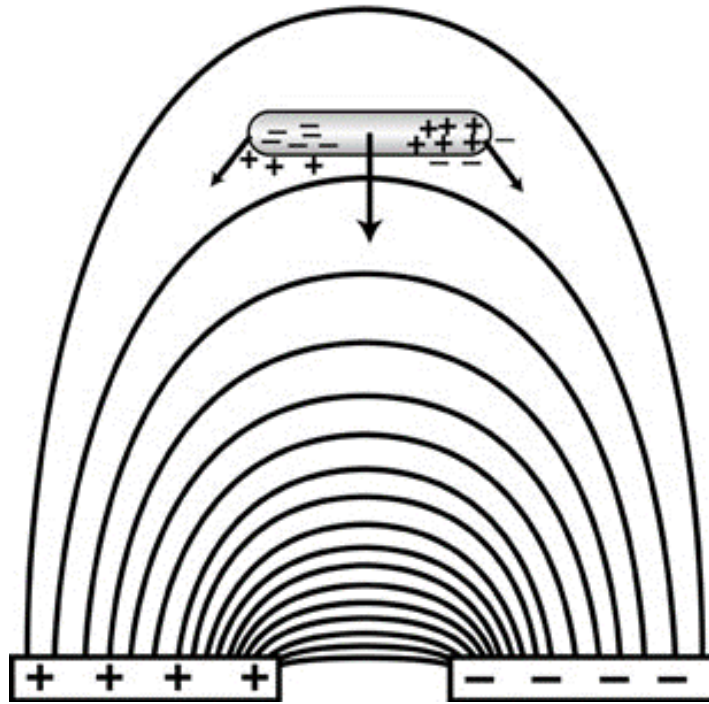
Figure 1: Illustration of a nanostructure subjected to dielectrophoresis. In this case, nanowire aligns with the electric field and experiences DEP force from the alternating field. Reproduced from [26] with permission of IOP Publishing.

Figure 1 illustrates the DEP deposition of a NT on to a pair of electrodes. Depending on the polarizability of the nanomaterial in comparison to that of the suspension medium, the nanomaterial can be pushed towards regions of high or low electric field, described as positive and negative DEP, respectively [17]. If the nanostructures are more polarizable than the suspension medium, the induced dipole along its longitudinal axis will experience dielectrophoretic force (DEP) that drives it to the electric field maxima. Positive DEP is experienced at frequencies below a characteristic threshold, which is termed as the

crossover frequency (Figure 1). If the nanostructures are less polarizable in comparison to the suspension medium, the induced dipole along its longitudinal axis will experience dielectrophoretic force which drives it towards the region of electric field minima. This negative DEP regime is experienced above the crossover frequency.

Using an approximation of NW as a prolate ellipsoid with length (major axis) much greater than its diameter (minor axis) in this model, the time-averaged value of the DEP force acting on NW is given by the following equation:

$$F_{DEP} = \frac{3}{2}\pi r^2 l \varepsilon_m Re\{K\}\nabla(E.E^*) \tag{1.1}$$

where, r, E, E^* denote the NW radius, applied electric field and complex conjugate of electric field, respectively. In this equation, frequency dependency of the dielectrophoretic force is described by K or the Claussius-Mossotti factor (CM factor). CM factor specifies the relative polarizability of nanowire with respect to the medium and is defined as:

$$K = \frac{\tilde{\varepsilon}_{NW} - \tilde{\varepsilon}_m}{\check{\varepsilon}_m} \tag{1.2}$$

where, $\tilde{\varepsilon}_{NW}$ and $\tilde{\varepsilon}_m$ are the complex permittivity of the NW and the suspension medium, respectively. The complex permittivity of the NW and medium are calculated from their real dielectric permittivity (ε), conductivity (σ) and field frequency (ω), as given below:

$$\tilde{\varepsilon} = \varepsilon - i\frac{\sigma}{\omega} \tag{1.3}$$

In Figure 2, the Claussius-Mossotti factor is shown as a function of excitation frequency for α-MnO$_2$ NWs in ethanol [17]. When the CM factor is positive, NWs are more polarizable than suspension medium and are attracted in the direction of the electric field maxima due to positive DEP. According to previous research, it has been shown that operating in the near but, sub-threshold regime of the crossover frequency provides the best potential for manipulating individual nanowires for effective capturing on the

4

electrodes [17]. Therefore, an excitation frequency of 1 MHz for both the model and the experiment were used for this thesis.
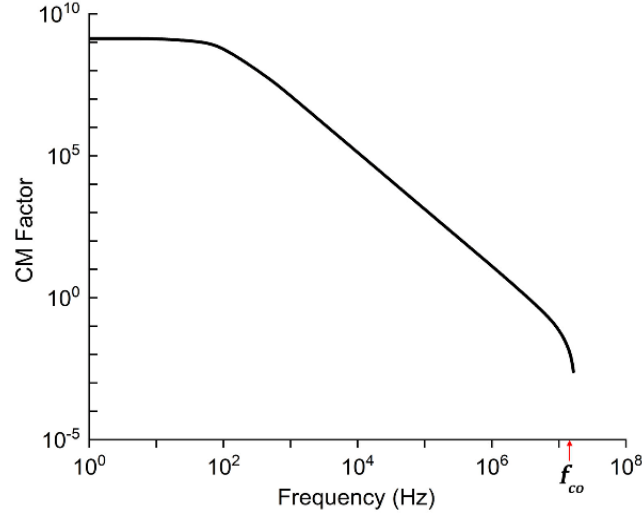
Figure 2: Claussius-Mossotti factor as a function of frequency. Reproduced from [17] with permission of The Royal Society of Chemistry.

Assuming a spatially invariant phase and a constant magnitude of electric field along the length of the NW, the dielectrophoretic force on the prolate ellipsoid shaped NW can be rewritten as:

$$F_{DEP} = \frac{3}{2}\pi r^2 l\varepsilon_m Re\{K\}\nabla|E|^2 \tag{1.4}$$

The above equation will be implemented in the numerical code to find the dielectrophoretic forces in the computational model.

Furthermore, the velocity of the NW (v) at any point in the field is calculated using following equation as:

$$v = \frac{F_{DEP}}{f} \tag{1.5}$$

where, F_{DEP} and f are the dielectrophoretic force and friction factor, respectively. This equation allows the calculation of velocity fields, which exist within the FE-DEP simulation workspace for a NW with a given size.

This velocity of the NW (v) at any point in the field is dependent on the interaction of the DEP force with the friction force. The NW inertial effects are neglected in this model because the experimental NW capture time is significantly larger than the characteristic time constant for inertial effects. In the above equation, the average friction factor for the NWs is calculated based on hydrodynamic models developed by Hardings and Small, and is given as [17]:

$$f = \frac{3\pi\eta l}{\ln(l/r)} \tag{1.6}$$

where, η is the viscosity of suspension medium (ethanol).

1.3 Floating Electrode Dielectrophoresis

Conventional or classic dielectrophoresis (C-DEP) [9, 26-27] utilizes two electrode designs where the electric field is generated on the opposing electrode pairs by applying an electric bias between them (Figure 3). In contrast, floating electrode dielectrophoresis (FE-DEP) [1, 5, 17-18, 29] uses a structure with one lower substrate electrode and two isolated top electrodes. One of the electrodes is connected to the bias potential while the opposing electrodes are kept floating. These electrodes are held at a floating potential with respect to the lower substrate, which acts as a third electrode and is electrically grounded. Thus, an additional capacitive impedance between the ground and floating electrodes is introduced to the electrical circuit during FE-DEP. This additional impedance grows in significance as NWs are deposited at the assembly site, thus significantly slowing down the capture of NWs beyond the first deposition. Over the years, FE-DEP has demonstrated relatively better control for nanoassembly than C-DEP. Experimental

findings have shown that the technique aided by FE-DEP improves the orientation and positioning precision and attains directional deposition of nanostructures on multiple electrode sites [17, 29-30].
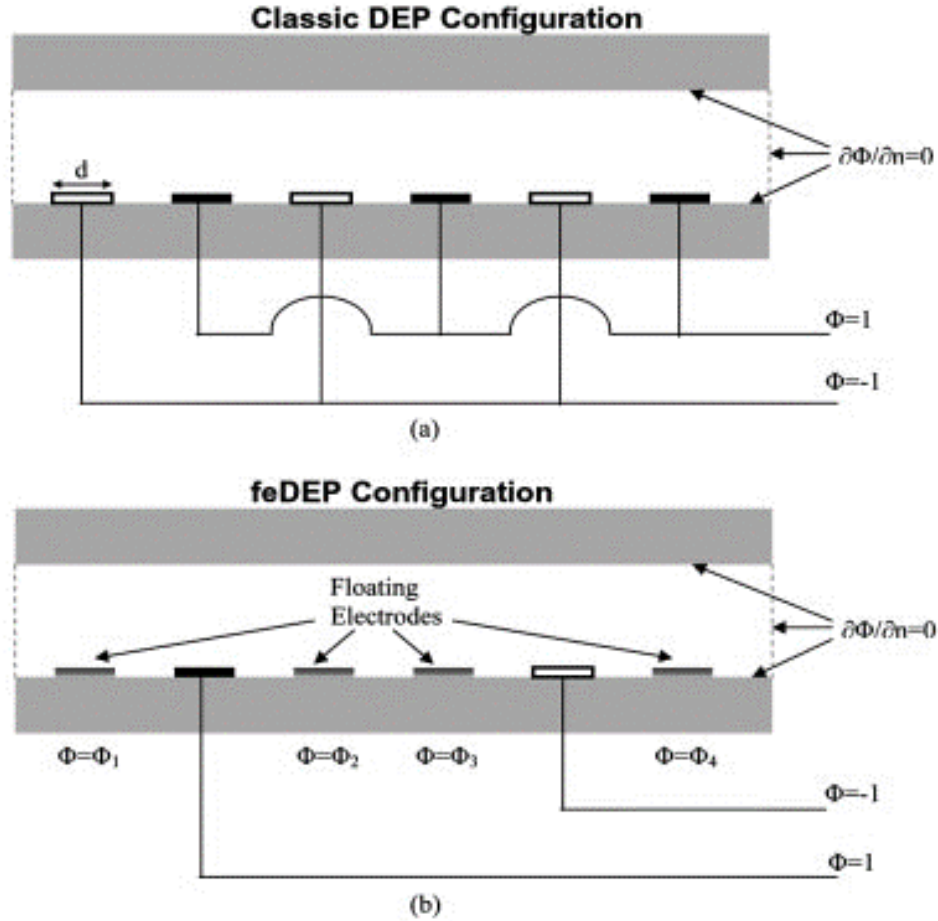
Figure 3: Models used in finite element calculations in; (a) classic DEP configuration, (b) Floating electrode DEP (FE-DEP) configuration. Reproduced from [31] with permission of John Wiley and Sons.

Taking the above-mentioned findings into consideration, the work presented in this thesis used FE-DEP. As shown in Figure 3 (a), all electrodes are excited in C-DEP configuration, and the applied AC voltages have similar amplitude. However, in FE-DEP configuration, the potential is applied only at two excited electrodes while the phase sequence of a quarter cycle is applied. The floating electrodes act as perfect electrical conductors and impose zero tangential electric field. As seen in Figure 3 (b), each floating electrode has unique potential and the net charge on each floating electrode is zero, since there is no charge transfer between electrodes.

7

1.4 <u>Problem Statement</u>

The field of dielectrophoretic device integration presents opportunities from innovative materials to promising applications. An eventual goal stands to produce extremely minute functional devices with high throughout, low costs and low operational power. Thus, a comprehensive numerical study which can predict NW trajectory from the imposed AC potential in dielectrophoretic regime will enable better understanding for large-scale device integration. Though there have been a few experimental reports on the use of FE-DEP [1, 5, 17-18, 29], there has been no quantitative three-dimensional modeling of FE-DEP. This comprehensive numerical study is vital, as it offers a model for predictive assembly of nanowires that accounts for all the process parameters such as size of NW, starting location of NW, suspension concentration, design of electrodes, applied electric field, and deposition time.

Therefore, the main objective of the present thesis is to develop a 3-D electrokinetic model, that calculates the imposed electric field and its resultant NW force/velocity maps within the region of influence of an electrode array operating in the FE-DEP configuration.

To achieve the objective, following steps were employed:

1. A 3-D electrokinetic model is employed to compute the nanowire trajectories and deposition sites using dielectrophoresis on the electrodes.
2. The electrokinetic model is further employed to predict the starting location for each assembled nanowire and to estimate its trajectory.
3. The accuracy of the introduced numerical model is demonstrated by comparing it with experimental results.

1.5 <u>Thesis Organization</u>

The thesis is divided into six chapters. In chapter two, device fabrication, dielectrophoretic assembly, and post-DEP image analysis procedures are presented. In addition, description of the design

parameters, boundary conditions, geometry and simplifying assumptions used in the 3-D Finite Element Model (FEM) are also presented.

Chapter three describes in detail, the process of creating the 3-D finite element models for the analysis of electric fields generated by electrodes, using COMSOL Multiphysics software. This chapter contains the description of material properties, geometry, boundary conditions, loading, meshing and solution.

Chapter four includes the MATLAB computations performed to convert electric field distribution into DEP force acting within the workspace region, using MATLAB software. The methodology for MATLAB code, various inputs used, and computation of DEP force is described in detail. Additionally, the approach for calculation of the NW trajectory, its eventual trapping location and NW mass concentration for each electrode pair is also shown.

Chapter five summarizes the experimental results obtained for two different deposition conditions. Also, the validity of the modeling approach is demonstrated by comparison of predicted NW mass concentration for all electrode pairs from both the experiments.

Lastly, in chapter six the conclusions are summarized.

2   DESIGN PARAMETERS AND EXPERIMENTAL PROCEDURE

To achieve the objective of this thesis an experiment was performed using the theory presented in chapter 1. NWs were deposited using FE-DEP on the nanoelectrodes, after which the final location of the deposited NWs and other parameters were determined for use in the 3-D electrokinetic model. This chapter of the thesis comprises of details related to the experimentation and experimental data analysis procedures. This is followed by a description of the design parameters, boundary conditions, geometry, and simplifying assumptions used in the 3-D Finite Element Model (FEM).

2.1 Device Fabrication and Experiment Procedure

The device nanofabrication process uses a combination of top-down silicon manufacturing and bottom-up dielectrophoretic (DEP) nanoassembly techniques (Figure 4). A silicon chip measuring 4mm x 6mm was used for fabrication of electrodes. The top layer of this chip acts as the starting substrate and has an insulating layer of 100 nm thick Silicon-Nitride (Si_3N_4) film. The gold nanoelectrode pairs were fabricated on top of this substrate.

The fabrication of gold nanoelectrode pairs was performed using a two-step process. In the first step, photolithography was followed by metal deposition and lift-off to form the large contact pads. Next, the gold nanoelectrode pairs are deposited in arrays using a combination of electron beam lithography (EBL) and metal lift-off. This prepared device with gold nanoelectrodes will be used further for the DEP experiments.
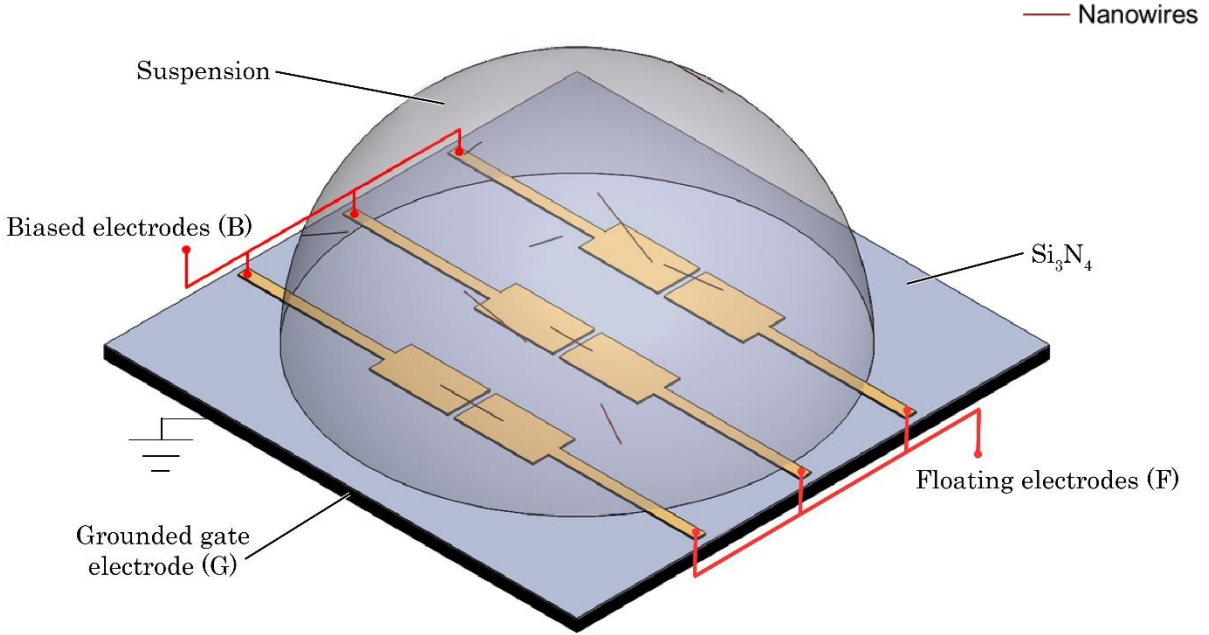
Figure 4: Schematic figure of on-chip DEP platform. The platform shows the floating electrodes (F), biasing electrode (B), grounded electrodes (G), apart from the substrate (Si_3N_4) and electrode pairs. The suspension including the NWs on top of electrode pairs is also illustrated.

The electrodes on one side of array were all connected to a common DEP bias with the large left pad, while the backside silicon substrate was subjected to AC ground (Figure 4). All the opposing electrodes were traced back to their individual pads and were maintained at a floating potential in the experiment. α-MnO$_2$ NWs synthesized by Dr. Ekaterina Pomerantseva's Lab at Drexel University were used as the model one-dimensional nanomaterial system for this study. A homogenous suspension of these α-Mn0$_2$ NWs was prepared by ultrasonication of the NW powder in ethanol. To deposit NWs on the nanoelectrodes, this suspension of NWs in ethanol, was placed on the silicon chip and an AC electric field bias (V$_{AC}$) was applied across the gold nanoelectrode array. A non-uniform electric field is generated around the electrodes due to the applied AC field. The electric field polarizes NWs in the suspension medium and results in an electrokinetic force. Nanowires are attracted in the direction of the electric field maxima due to the resulting DEP force, thereby depositing them across the electrodes (Figure 1). As shown in Figure 4, the left-side

electrode is called the biasing (B) electrode, while the other is called the floating (F) electrode. Lastly, the underlying silicon substrate is connected to the ground and is called gate (G) electrode.

After the predetermined experiment time of 2 minutes, the assembly bias was turned off and the silicon chip was rinsed thoroughly in ethanol, after which it was dried using Nitrogen (N_2) gun. The NWs stayed secured on the chip due to Van der Waals forces. In the first experiment, an excitation frequency of 1 MHz, deposition time of 2 minutes, and a bias voltage of 1.5 V_{p-p} (Voltage from peak to peak) was maintained. In the second experiment, the deposition time and excitation frequency remained at 2 minutes and 1 MHz respectively, while the voltage is changed to 2 V_{p-p}. In both experiments, an array of 49 electrode pairs was monitored after the assembly process.

Afterwards, the chip was imaged in a scanning electron microscope (SEM). These images were acquired at each of the 49 electrode pairs after DEP assisted assembly. These images were processed to obtain the post-assembly deposition locations of NWs for each deposition condition and serve as a key input to validate the accuracy of the model developed in this thesis (to be discussed later). The FE-DEP experiments and imaging for this research were performed by Md Ruhul Amin Shikder, a research collaborator at the UIC Laboratory for Integrated Nanosystems.

The equivalent electrical circuit for the DEP system consists of three impedance components in series, as depicted in Figure 5. As seen in this figure, the electrical circuit contains the following impedances:

1. The capacitive coupling between gate and floating electrodes (Z_{F-G}).
2. Impedance contribution by suspension between bias and floating electrodes (Z_{susp}).
3. Double layer capacitance contributions between electrodes and suspension, which is shown by the impedance terms (Z_{B-DL} and Z_{F-DL}).

The effective assembly bias (V_{DEP}) used in the DEP experiments is determined by the relative magnitudes of these impedances.
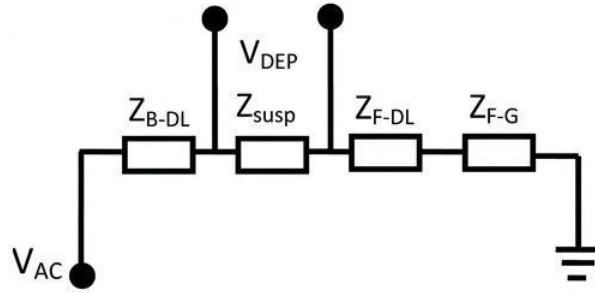
Figure 5: Equivalent electrical circuit showing the impedances and effective DEP bias. Reproduced from [17] with permission of The Royal Society of Chemistry.

2.2 Image Processing

Determining the final position for each of the deposited NWs is a required piece of input information for validating the FEM model. For this purpose, the SEM images were analyzed using NIH ImageJ software. To determine the precise location of the deposited NWs, the SEM images were first straightened to align all the SEM images identically, followed by calibration to be identical with the origin. The calibration and alignment was performed for all the SEM images to keep the reference of final deposited NWs similar for computation. After calibration and alignment, the scale was set using known distance in pixels. Using multi-point tool, all the ends of NWs were mapped and measured. The data from these measurements was exported to Microsoft Excel and the angle, length and final location coordinates of deposited NWs for each SEM image was recorded. The optical and SEM images of the on-chip nanoelectrodes array on silicon chip before and after the DEP is shown in Figure 6 (a-b), respectively.
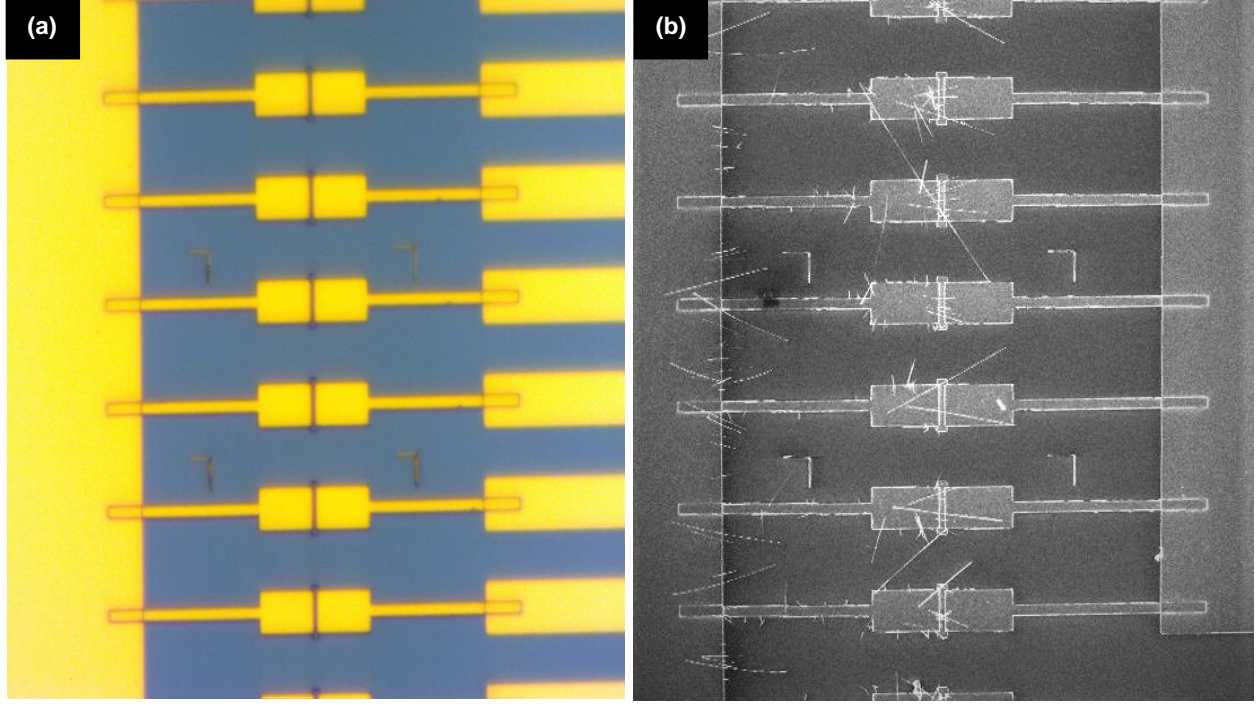
Figure 6: (a) An optical microscopy image of the nanoelectrode array on silicon chip, (b) SEM image showing deposited NWs after DEP experiments on the nanoelectrode array.

2.3 <u>Boundary Conditions for the 3-D FEM</u>

Applying appropriate boundary conditions in the FE model is a key requirement to insure its accuracy. There are several boundary conditions that are applied, and these are discussed below.

2.3.1 <u>Boundary Conditions</u>

At the upper bound, where the heights are much greater than the typical electrode dimension, both the electric field and the potential approach zero. Additionally, the upper boundary is adequately distant enough from the electrodes. Therefore, either a Dirichlet boundary condition $(\phi = 0)$ or the Neumann boundary condition $\left(\frac{\partial \phi}{\partial n}\right) = 0$ can be specified for the numerical problem [32]. For the simulation in this thesis, Neumann boundary condition was assigned.

In the electrical domain, the left and right boundaries along with the remainder of the lower boundary represents the interface between the suspension above the electrode. At this interface both the normal component of total current (displacement and conduction) and the potential are continuous. Therefore, the Neumann boundary condition $\left(\frac{\partial \phi}{\partial n}\right) = 0$ was used. The normal derivative of the potential is zero on the bottom of the channel, along the gap between adjacent electrodes. Furthermore, the simulations are limited to an isolated electrode pair and the impact of the neighboring electrode pairs in the array is accounted within the model using a symmetric boundary condition (Figure 7). This boundary condition was applied on exterior boundaries of the model, to limit the computational cost and reduce the overall time of the simulation.
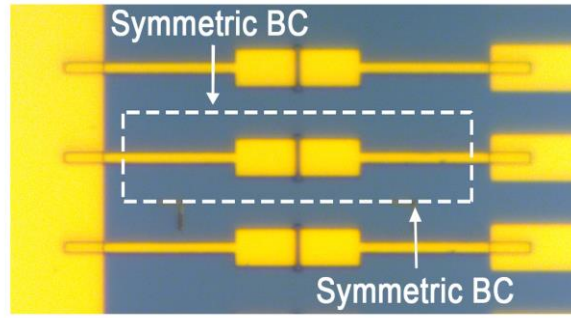
Figure 7: A 3-D unit cell is utilized as the simulation workspace with symmetric boundary condition applied. It contains a single electrode pair and extends up to the mid-point of its separation region with respect to the neighboring electrode pairs in 3-D workspace.

2.3.2 <u>Applying Loads for FE-DEP</u>

The potential in FE-DEP configuration was only applied at the two excited electrodes. They are modeled as perfect conductors, are equipotential and impose zero tangential electric field. The floating potential was applied on one of the electrodes, while the biasing potential value was applied on the other electrode. Biasing potential value for the electrodes differed for the two models from 2 V to 1.5 V, as used in the experiments.

2.4 Design Parameters, Geometry Considerations and Simplifying Assumptions

Two different chips were fabricated with the same geometry to perform the DEP experiments. The electrode geometry was replicated in the computational models. Specifically, each electrode was 7.5 μm long, 4 μm wide and 150 nm in height. The electrodes were separated by a 600 nm gap. The simulation workspace was chosen as a 3-D cuboidal unit cell that extended up to 20 μm in height from the electrode surface.

Besides the geometric simplification made using symmetry, the contributions of inertial effects were also neglected in the model. These effects were neglected as the characteristic time constant for motion due to inertial effects are negligible compared to that of the DEP forces.

3   COMSOL MODELING

Three-dimensional finite element models were created for the analysis of electric fields generated by electrodes, using COMSOL Multiphysics software (version 5.3a). Results obtained from the finite element analysis (FEA) were taken to the MATLAB environment in order to predict the trajectories of deposited NWs and to calculate the NW mass concentration in the homogenized suspension. Finally, the predicted NW mass concentration for all the electrode pairs is checked for homogeneity to validate the computational models. The contents of this chapter discuss the finite element model (FEM) and its outputs.

To initiate the model, the electrostatic interface was chosen from the AC/DC branch of COMSOL physics environment. Employing scalar electric potential as a dependent variable, the physics interface solves the Gauss's law for electric field distribution. This process involves appropriate material selection as used in the experiments. Geometry was defined accurately based on the SEM images. Since, both chips have the same geometry, only the loading condition (voltage) was changed while keeping the model constant.

The boundary conditions were then applied in the electrostatic physics interface. A mapped mesh was created by building a meshing sequence. This sequence contained several meshing operations on the domain to create a uniform quadrilateral mesh.

Finally, the output was generated and the data was exported into MATLAB. The FE model for this research were created by Sachin Kumar Singh, a research collaborator at the UIC Laboratory for Integrated Nanosystems.

3.1 <u>Material Properties</u>

3.1.1 <u>Silicon-Nitride</u>

Silicon-Nitride (Si_3N_4) is the base substrate for the electrodes. To simulate the Si_3N_4 material, a relative permittivity of 7.5 was used. Only the bottom surface of the geometry in our simulation was attributed to Si_3N_4 properties.

3.1.2 <u>Ethanol</u>

The homogenous suspension of NWs was prepared in ethanol. The non-uniform electric field was generated within this medium upon the application of AC field. A relative permittivity of 21.4, as used in past literature [17], was assigned for ethanol. The properties of ethanol were used for the whole geometry besides the bottom surface where the Si_3N_4 substrate is present.

3.2 <u>Geometry</u>

After assigning the material properties, geometry of the experimental DEP chip was replicated in the FE model by careful measurement of the chip dimensions using the SEM image. As mentioned in the previous chapter, for both experimental conditions (which were simulated in this thesis), the geometry is similar. Furthermore, the model geometry was divided into four different domains, as listed below (Figure 8):

a. Upper domain: This region is located farther away from the electrode pairs and hence, does not require a high-density mesh.

b. Lower domain: This region includes the volume from which NWs are sourced for assembly and is hence, meshed with a higher density of elements in order to ensure accuracy of results.

c. Electrodes and the Electrode connectors.

d. Si_3N_4 layer: This layer consists of the Si_3N_4 pad and the Si_3N_4 gap, which is the base substrate on top of which the nanoelectrodes are manufactured.

Consequently, the final object was built by forming a union of each geometric domain listed above. This union from all geometric objects, which were divided into constituent domains, were separated by boundaries. The physical implication of the union step is that the domains in the model cannot slide or move relative to each other.
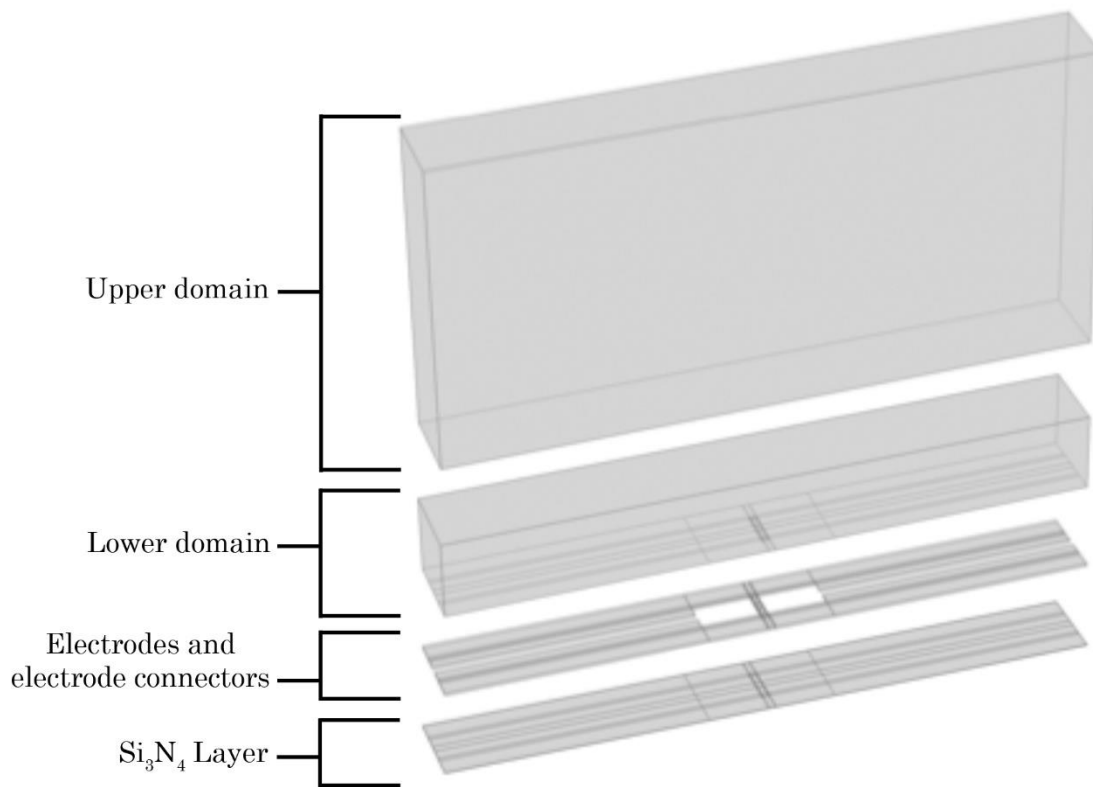

Figure 8: The partitions of different domains on the geometry for the three-dimensional model of FEM.

3.3 <u>Boundary Conditions</u>

Appropriate boundary conditions are essential to achieve accurate results. The following sections detail the boundary conditions used in the FE model.

3.3.1 <u>Charge Conservation</u>

Including the boundary condition of charge conservation defines the equation for electric potential and allows defining the constitutive relationship for the Gauss's law for the electric field displacement shown in the below equations:

$$E = -\nabla V \tag{1.7}$$

$$\nabla \cdot (\varepsilon_o \varepsilon_r E) = \rho_v \tag{1.8}$$

where, E is the electric field, V is the electric potential, ε_r is the relative permittivity, ε_o is the permittivity of vacuum and ρ_v is the space charge density. This condition was specified using the charge conservation throughout the domain in the simulation. At the interior interface between the domains, both the normal component of total current (displacement and conduction) and the potential are continuous. As discussed in the previous chapter, for this simulation the Neumann boundary condition $\left(\frac{\partial \phi}{\partial n}\right) = 0$ was assigned by default in COMSOL.

3.3.2 <u>Zero Charge</u>

Zero charge boundary condition implies that there is no charge at the boundary and it involves the following equation:

$$n \cdot D = 0 \tag{1.9}$$

where, n is the outward normal and D is the electric displacement. Since the potential is symmetric with respect to the boundaries, the symmetric boundary condition was applied in the FE model using the zero-charge boundary condition at the exterior boundaries.

3.4 <u>Loading</u>

Defining and applying loads on the electrodes was the next step in the modeling process. In general, two kinds of potentials were applied: electric potential (assembly bias) and floating potential. These are key parameters that determines the electric field, which will be utilized later in MATLAB computations. This electric potential load was applied at the boundary of the left electrode and its connector using the *electric potential option*. The voltage applied was 2 V in the first model and 1.5 V in the second model, which was the same as the values used in experiments. Correspondingly, the floating potential was applied to the boundary of the right electrode and its connector.

3.5 <u>Meshing</u>

All of the domains were chosen as dependent parts in order to perform meshing at the boundary and domain level. The *size option* was used to discretize the model into small elements. The number, size and distribution of the elements was controlled using the *size option*. To keep the mesh consistent, a quadrilateral mesh was chosen. *Mapped option* was utilized to create a structured quadrilateral mesh for each domain. The final mesh obtained from the model is shown in Figure 9.

As seen in Figure 9, the lower domain above the electrodes had denser meshing and the distribution of the elements gets finer to coarser, as it moves away from the electrode. This exponential element distribution was obtained using element ratio and geometric sequence setting in the *distribution option*. Coarse mesh was applied at regions that were projected to have low electric field levels (like the upper domain, which is at the far end of from the electrodes). Finally, after defining all the settings and distribution, the swept option was used to sweep the mesh using distribution from the source face to the destination face.

21
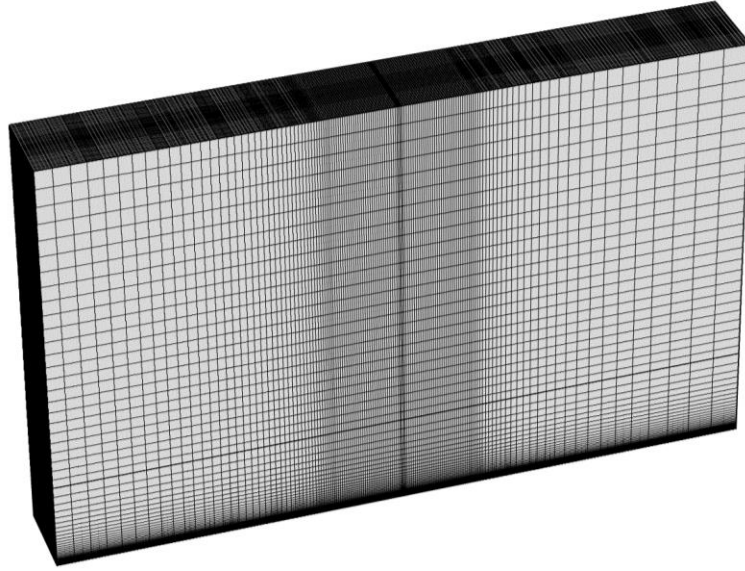
Figure 9: The quadrilateral mesh used for all domains of the geometry. Note that the mesh gets coarser as it moves away from the electrode pair.

3.6 Solution

After defining the geometry, material properties, boundary conditions and loading, the final step was to compute the solution. This was done by using *study option*, which solves the model at all the nodes. After solving the FEM, the essential solution outputs like electric field distribution and electric potential were obtained. Figure 10 (a-b) shows the top and side view of the electric potential and normalized electric field distribution around the electrode pair. Note that the electric field vectors originate from the biasing electrode and terminate at the grounded silicon substrate. In addition, the electric field maxima is asymmetrically located in the inter-electrode gap region and remains near the edges of the biasing electrode (left electrode). Furthermore, the normalized force vectors within the simulation workspace are shown in Figure 10 (c) and in this figure, it can be seen that the force vectors are attracted towards either the biasing electrode (left side) or the electrode gap.

Finally, after solving the FEM, electric field distribution results were exported to MATLAB, to perform dielectrophoretic force and NW response calculations. This electric field distribution result included the following:

1. Normal electric field (V/m),

2. Electric field components in x, y and z directions, and

3. Gradient of the square of the electric field in x, y and z directions.
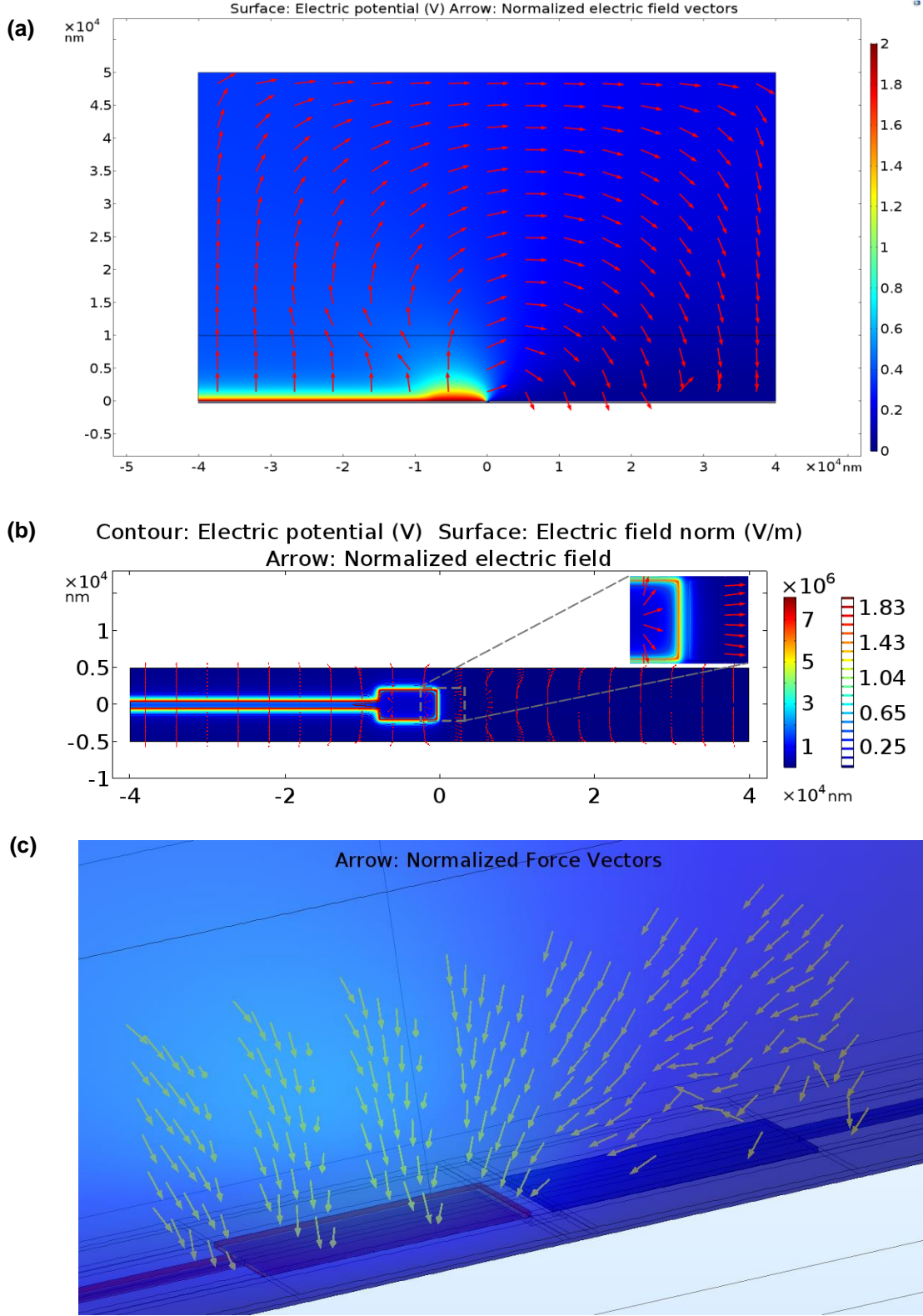
Figure 10: (a) Side view of computed electric field in FE-DEP domain using COMSOL 5.3a, (b) Top view of the computed electric field distribution at plane which passes through the electrode center line, (c) Normalized forced vectors showing the direction of NW motion during FE-DEP assisted assembly.

4 MATLAB COMPUTATIONS

The data computed for all the nodes from the FE simulation was imported as an input to the MATLAB R2017b environment. The MATLAB code was used to compute the trajectories of the NWs within the electrokinetic field. This was achieved by using the velocity map computed in MATLAB (using equations (1.1-1.6)). This MATLAB code converts the computed electric field distribution into the DEP force within the simulation workspace. The numerical code, which was first developed by Sachin K. Singh (a research collaborator at the UIC Laboratory for Integrated Nanosystems), was further modified to achieve the objective of this thesis.

4.1 <u>MATLAB Code Methodology</u>

For the numerical code, the output mesh data file with computed electric field distribution components from the FEA for various nodes, was one of the inputs. All input parameters used in the MATLAB script are explained in section 4.2. Since the input from COMSOL gives repeating nodes, which can cause errors and discontinuity during the post processing, it was essential to average out the repeating nodes from input of the FEM solution. This output mesh data was then sorted and stored based on location in the z- direction, then based on the location in the y- direction, and finally the x- direction to break ties.

Subsequently, the DEP force components in x-, y- and z- directions for each individual node were calculated (based on equation (1.4)). Using these DEP force components and the average friction factor, the velocity at each node in the domain was calculated (using equations (1.5-1.6)). As a result, velocity field distribution for a NW, which exist within the FE-DEP workspace was generated. This velocity map was further used to calculate the NWs trajectory, eventual trapping location on electrode surface, and its deposition time within the FE-DEP simulation workspace. This step is explained in detail in section 4.3.

Furthermore, the code was extended to calculate the number of starting locations and the farthest possible starting locations from which NWs can be deposited, as explained later in section 4.4. Using these

farthest possible starting locations for deposited NWs, the volume enveloped was predicted using the model to calculate the concentration of NWs mass for a given electrode pair. This predicted NW mass concentration was used to evaluate the accuracy of the model.

4.2 <u>Inputs</u>

The input parameters are an important aspect of the numerical code. The data processing involved the following input parameters:

- x, y and z were the location of the nodes (n), in the three-dimensional (3-D) workspace.

- The radius (r) and axial length (l) of the NW in meters. The radius was kept constant at 10 nm, but the axial length was estimated from SEM images for each electrode pair. A nominal radius of 10 nm was assumed as it was at the mid-range of radii observed experimentally.

- The real permittivity (ε_m) of the medium was assumed as 2.17×10^{-10} F/m and the conductivity (σ_m) of the medium as 1.35×10^{-7} S/m. These values were taken for the suspension medium (ethanol) as discussed in chapter 1.

- The real permittivity (ε_{nw}) of the NW was assumed as 2.07×10^{-10} F/m and the conductivity (σ_{nw}) of the NW as 182.2 S/m [17].

- Angular frequency (ω) of the applied AC voltage in rad/s as mentioned in equation (1.3) of chapter 1. This was calculated using experimental excitation frequency of 1 MHz.

- $\tilde{\varepsilon}_m$ and $\tilde{\varepsilon}_{NW}$ were the complex permittivity of the suspension medium and NW in F/m. The value for complex permittivity is calculated using equation (1.3) from chapter 1.

- K was the Claussius-Mossotti factor and describes the frequency dependency of DEP force.

- θ was the angle of orientation of the electric field in the planar workspace.

- η was the viscosity of the suspension medium (Ethanol). This is used to calculate the friction factor and to calculate the velocity maps in the numerical code.

- E_x, E_y and E_z were electric field components in x, y and z directions respectively. These components were used to calculate the DEP force components in respective directions.

- $\nabla|E_x|^2, \nabla|E_y|^2$ and $\nabla|E_z|^2$ were squares of the x-, y-, and z- components of the electric field gradient. equation (1.4) was implemented using these components in the numerical code.

- To find the farthest starting location, L, X_c and Y_c were used as inputs. Here, L was the actual length of NW. X_c and Y_c were, x- and y- coordinates for the center of the NW. These inputs were calculated using SEM images as discussed in chapter 2.

- Finally, the average friction factor (f) was utilized to calculate the velocity using equation (1.6).

4.3 DEP Force and NW Trajectory Calculation

After all the necessary inputs are assigned, the MATLAB code was used to compute the DEP force and the trajectory of the NWs. Using equation (1.4), the DEP force field within the simulation workspace, was computed. The DEP force components in x, y and z directions for each individual node was calculated using equations (1.1-1.4). Finally, using the DEP force components and average friction factor, the velocity at each node in the domain was calculated using equations (1.5-1.6). Thus, the velocity field distribution, which exist within the FE-DEP workspace, is generated for any given NW.

This velocity map was further used, to calculate the time required for the NW to move from one node to its adjacent nodes in all directions. This movement of NW from one node to another is in 3-D space. The velocity vectors in x, y and z directions were sorted, then the time required for NW to move from one node to its adjacent nodes in all directions in 3-D space was calculated and stored. This was performed for each node in the domain and the smallest time for displacement along each direction was determined. Using this minimum time, the possibility for NWs to traverse more than 50% of the distance to its adjacent node

in other directions was examined. If it did pass this condition, then the NW was moved to the adjacent node
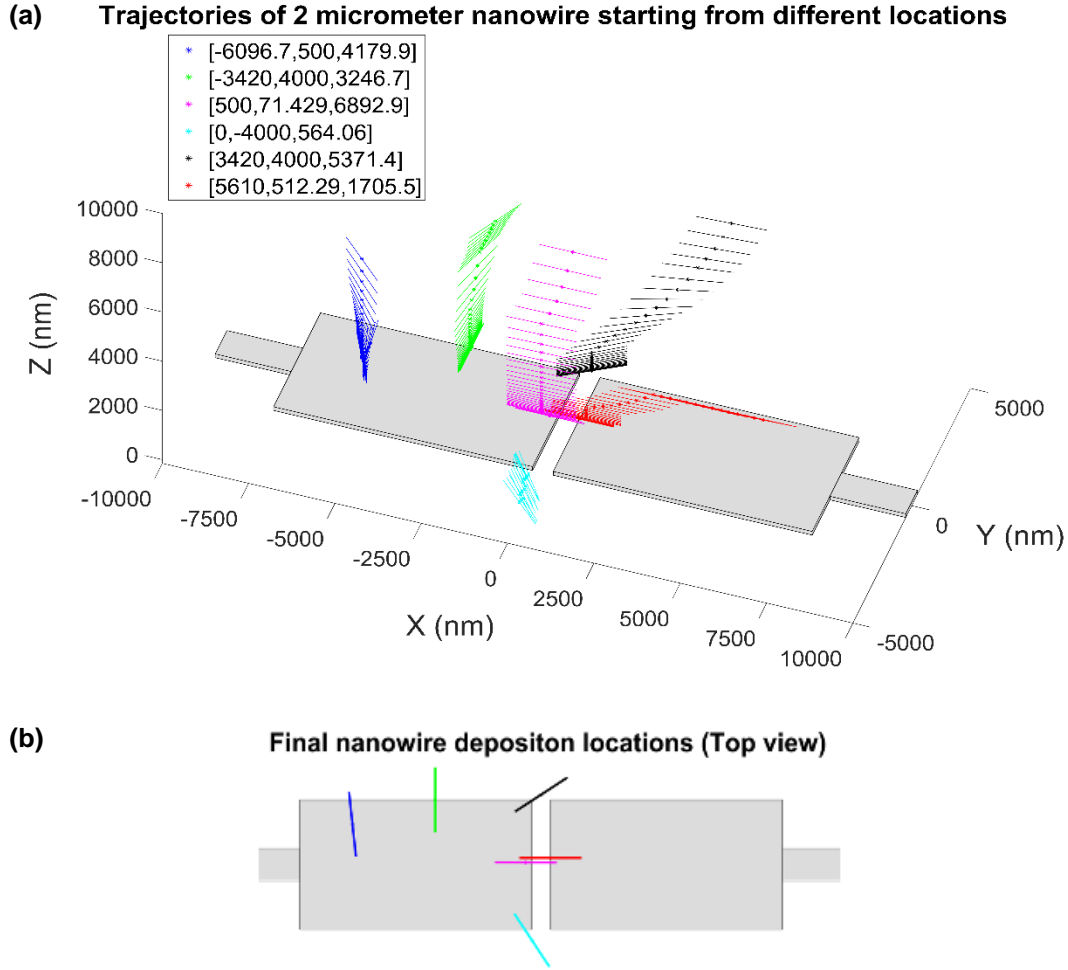
in all permitting directions.

Figure 11: (a) 3-D view of Trajectory of 2 μ m NWs starting from different locations in the domain, (b) top view of the final deposition locations. Note the impact of starting position on trajectory and final deposition location of NWs.

Since the NW trajectory was calculated for deposition on the electrode, the regional boundary limits

of NW deposition were defined. Finally, using these limits as the break condition for the loop, the motion

of a NW was stopped when it was deposited within this region of interest. The above mentioned method

was followed for every node and the time taken for deposition, initial node number, deposition node number

and the location were stored.

28

Figure 11 shows the trajectories assumed by a 2 μm long NW (with a radius of 10 nm) for six different starting locations in the DEP domain. In this figure, it can be observed that four out of six NW starting locations yield assembly on the biasing (left) electrode. This is because of the asymmetry in the FE-DEP electric-field gradient. The remaining two cases, which start from initial positions over the floating electrode, yield deposition across the electrode pair.

4.4 Farthest NW Starting Location and NW Concentration Calculation

Once the trajectory of the NW was evaluated, the code was extended to compute the farthest possible NW starting location for every deposition site. In addition, the localized NW mass concentration was estimated at each electrode site.

The trajectory calculations used a constant NW length and radius. But in the actual experiments, the NWs vary over a wide range in length. Consequently, the average friction factor also varies because of the change in length and radius of NW as described in equation (1.6). To accommodate these changes, the values for all deposited NWs were scaled with respect to the reference length of 2μm, which was used in the trajectory calculations code. After setting all the necessary inputs and scaling the length according to the experimental results, the farthest location from which a NW is attracted at each electrode site was computed. Using the deposition location of NWs from the SEM images, calculated as mentioned in chapter 2, the deposition node identical to the experimentally deposited NW location was found. Upon determining the deposition node in the numerical code, the data from the trajectory calculations was compared to find the starting node, deposition node and the deposition time. Using the coordinates of the starting node and the deposition node, the distance between the farthest location and the NW deposition location was calculated. The farthest location was specified using the x-, y-, and z- coordinates of the starting node.

After the farthest location calculation, the region of influence (outermost extent in the workspace from which the NWs can be successfully captured) was calculated. This region of influence (ROI) is defined

29

as the volume envelope for NW starting positions that yield deposition on the electrode pair within the specified time (2 minutes). This duration is the same as the value used in experimental tests. Additionally, the ROI includes deposition at both, the inter-electrode gap and single electrodes (biasing and floating electrode) regions within the specified time.

Figure 12 shows the ROI within the FE-DEP workspace from which NWs can be captured within a deposition time of 2 minutes. It can be observed that the electrode pair attracts NWs from regions over both the electrodes, even though only one of the electrodes is biased and the other is maintained at a floating potential. Moreover, the overall volume envelope for NW starting positions from which they are captured remains nearly symmetric with respect to the electrodes, even though NWs are predominantly deposited on the biasing electrode.
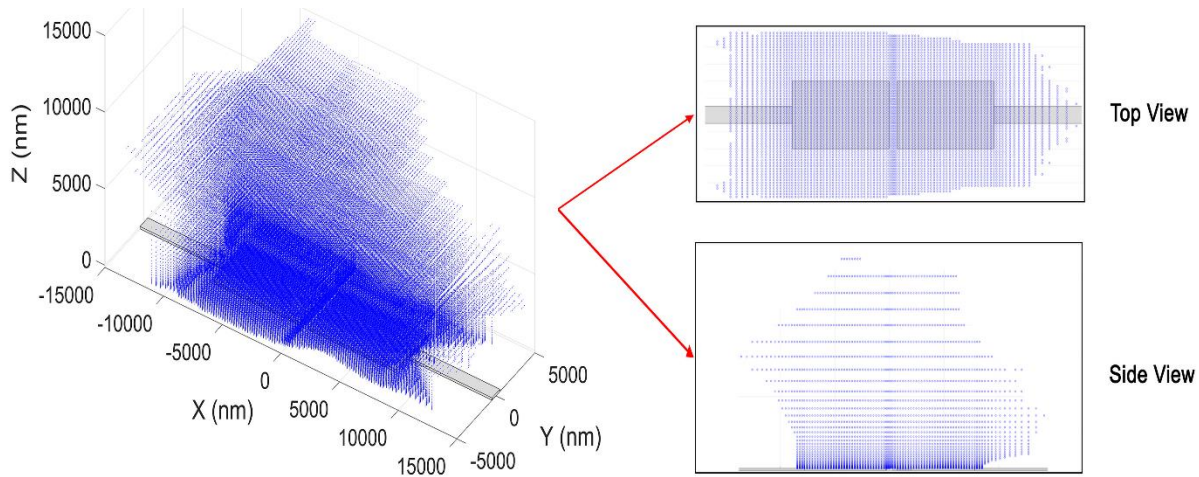

Figure 12: The region of influence (ROI) for a deposition time of 2 minutes.

Furthermore, the volume from which NWs are sourced for deposition at each electrode pair was determined. This volume for a given electrode pair was estimated by finding the region of 3-D workspace that envelops the farthest possible starting locations for each deposited NWs for the given electrode pair. The calculated volume is referred to as the local NW sourcing volume. The sourcing volume was calculated by fitting a hemisphere with the farthest starting points data for a given electrode pair by least square method. This was followed by determination of convex hull generated from X-Y coordinates of all the NW

starting locations. Finally, the space enclosed inside the outer boundary between the convex hull and fitted hemisphere was evaluated, giving the local NW sourcing volume. Figure 13 shows an example of the enveloped sourcing volume for the farthest location of deposited NWs. Note that the blue line on the X-Y plane depicts the convex hull created using x and y coordinates of starting locations of NWs. Moreover, the highlighted region shows the surface and outer boundary within which the volume is enclosed.

Lastly, the total mass of captured NWs at each electrode pair was determined using their crystallographic mass density (which is 4.34 g/cc for α-MnO$_2$ NWs [17]) and NW volumes (using the nominal radius of 10 nm and varying lengths calculated using SEM images). For both the experimental conditions, the NW sourcing volume, total mass of the deposited NWs and the corresponding NW mass concentration at each electrode pair were calculated.
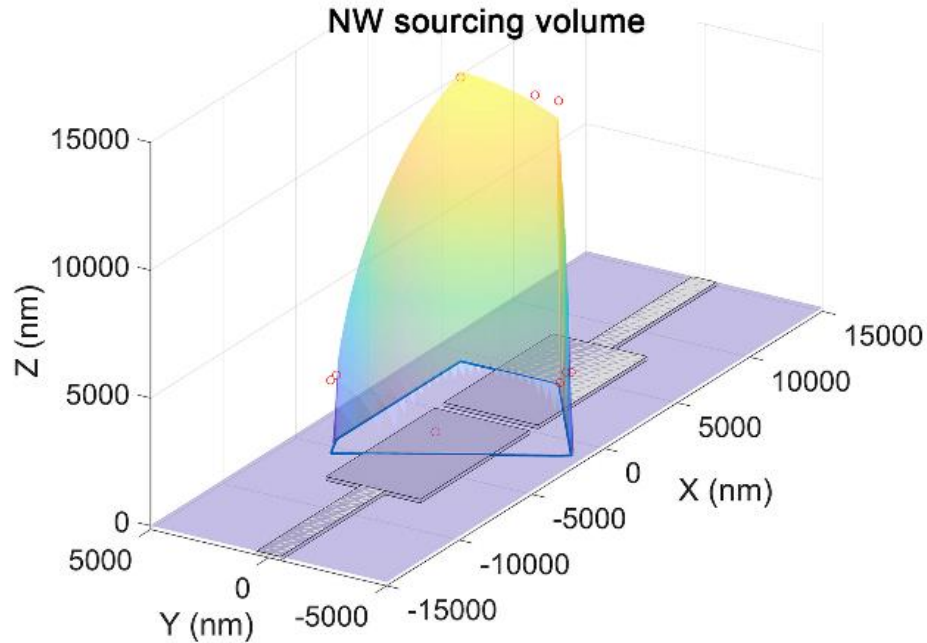

Figure 13: Example of predicted NW sourcing volume enveloped for the farthest locations of NWs deposited on electrode pair.

Since the same homogenized NW suspension was used for both the experiments, the NW mass concentration should ideally be identical for both the experimental conditions. Thus, the calculated NW mass concentration for both the experiments was compared to confirm the validity of the FE model.

5   RESULTS AND DISCUSSION

In this chapter, the experimental results for the two NW deposition conditions are summarized. Also, results from the comprehensive 3-D electrokinetic model, which was outlined in chapters 3 and 4 are presented. Furthermore, the simulation results are compared with the experimental data-set to validate its accuracy.

5.1 <u>Experimental Results</u>

After the DEP assisted assembly, the SEM images for 49 pair of electrodes for both deposition conditions (i.e., 1.5 V and 2 V bias, as explained previously) were analyzed. It was observed that NWs of varying lengths were deposited on electrode pairs. This is because, the colloidal suspension is created from ultrasonication of a NW powder containing different sized wires (varying predominantly between 1 μm to 12 μm, with very few NWs lying outside this range).

In Figure 14 (a), the length distribution for the 755 NWs, which were captured in total across all the 49 electrode pairs at 1.5 V deposition condition, is shown. In a similar fashion, the distribution for all the 875 NWs deposited on electrode pairs for 2 V bias is shown in Figure 14 (b). From Figure 14 (a-b), it is evident that the NW length ranges predominantly from 1 μm to 12 μm, where the occurrence frequency is highest for 2 μm NWs.
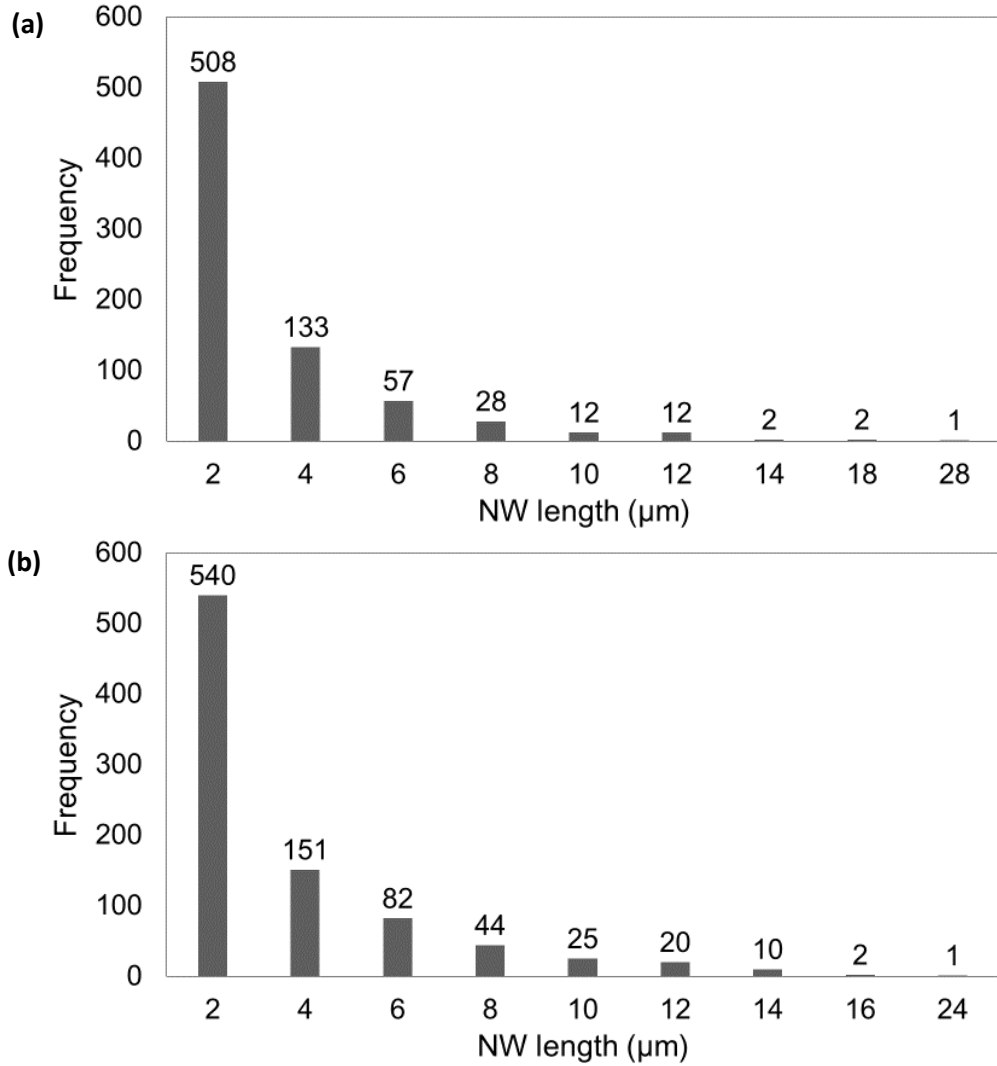
Figure 14: (a) Distribution of total number of deposited NWs according to length for 1.5 V bias, (b) Distribution of total number of deposited NWs according to length for 2 V bias.

Additionally, the total number of NWs deposited on each electrode pair for both the experiments were evaluated and compared. Figure 15 (a-b) depicts the total number of NWs deposited on each electrode for the two experiments. Note that the dotted line in the graph indicates the average NWs deposited on the 49 electrode pairs in both experiments. While an average of 13.26 NWs per electrode pair was found in the case of 1.5 V bias, an average of 17.85 NWs per electrode pair was found in the case of 2 V bias. This is in

accordance with the model, as a larger ROI is created due to higher bias and results in the trapping of a larger number of NWs on the electrode pairs.
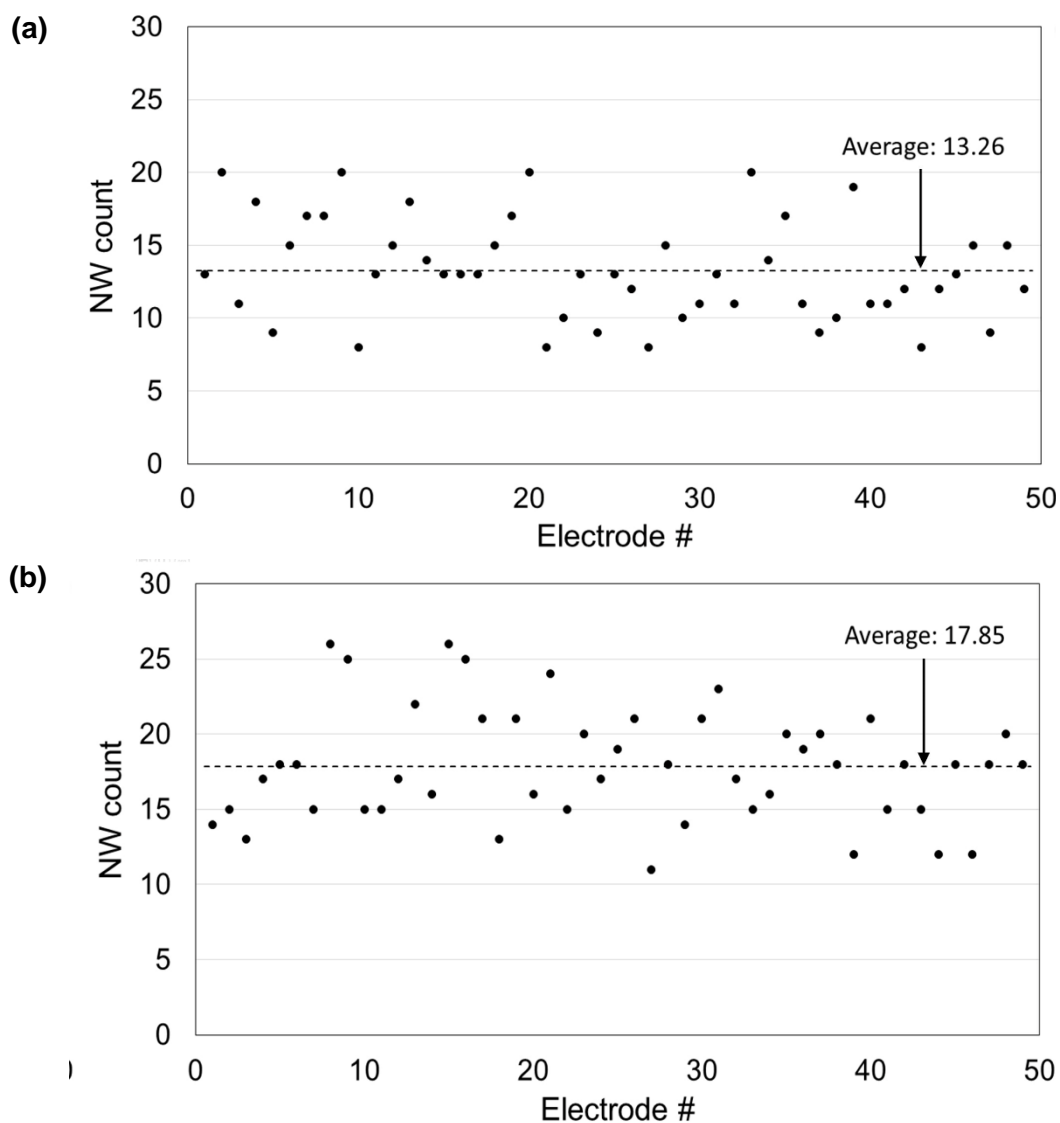

Figure 15: (a) Variation in number of NWs deposited on electrode pairs for 1.5 V bias, (b) Variation in number of NWs deposited on electrode pairs for 2 V bias.

5.2 <u>Effect of DEP Parameters on NW Deposition</u>

Next, the impact of FE-DEP parameters like biasing voltage, deposition time, NW lengths and starting positions on the deposition process was examined. This was done by investigating the NWs captured at the center of an electrode pair as a function of the deposition time.
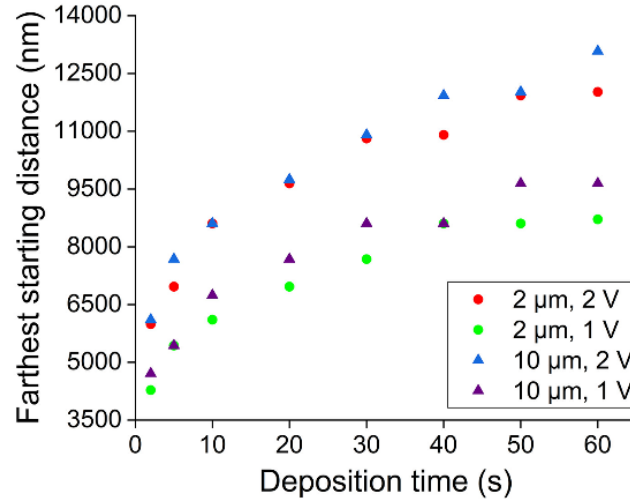

Figure 16: Effect of voltage, NW size and deposition time on the farthest distance from which NWs can be deposited at the center of electrode pair (0 μ m, 0 μ m).

As seen in Figure 16, the farthest starting distance from which NWs can be captured increases with an increase in deposition time and applied voltage. This is expected because DEP force is directly proportional to the square of electric field and therefore, the farthest starting distance increases with increase in voltage, as can be seen from equation (1.4).

On the other hand, the progressive increase in farthest starting distance recedes with an increase in deposition time. This happens because the force diminishes with increasing distance from the electrode pair. With this increasing distance, the velocity at farther points is reduced. Note that the farthest starting distance from which a NW can be attracted is not greatly influenced by an increase in NW length. This is because the NW velocity is proportional to the logarithm of its length-to-radius ratio (based on equations (1.5-1.6)) Since, the radius is constant for both the conditions, the velocity increases only by 30% with an increase in NW length from 2 μm to 10 μm.

5.3 <u>Finite Element Validation</u>

To check the validity of the modeling approach, the experimental data was compared with the numerical results. This was done by comparing the estimated NW mass concentration for both the experimental conditions.

Since the same homogenized NW suspension was simultaneously used for both the experiments, the computed NW mass concentration from the model should ideally be the same for both cases. The overall mass concentration of NWs in the homogenized suspension is anticipated to remain nearly the same at every electrode site and every deposition condition.

5.3.1 <u>Modeling Results</u>

After the SEM images for 49 pair of electrodes for both the conditions (1.5 V and 2 V bias) were analyzed, the results from the FEA and experiments were compared for each of the electrode pair.
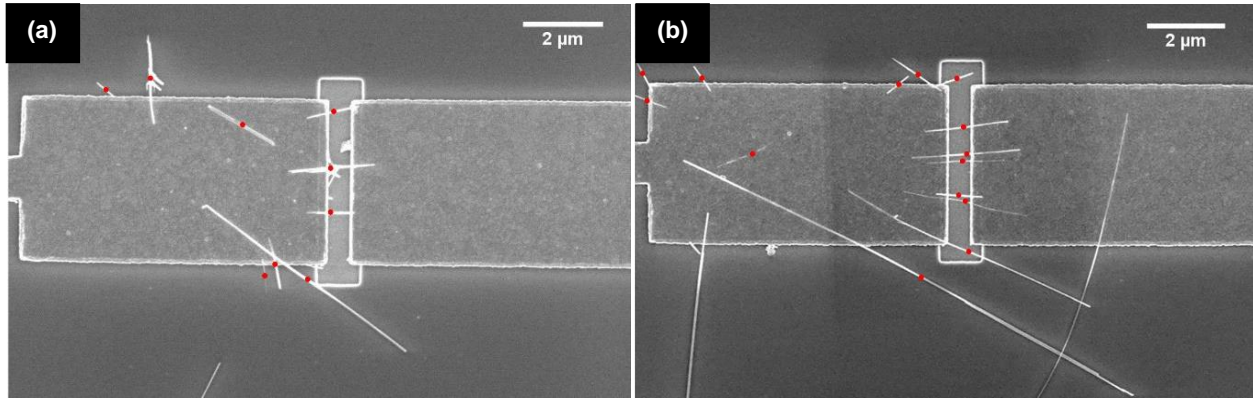

Figure 17: (a-b) SEM image showing deposited NWs for 1.5 V bias and 2 V assembly bias, respectively. Note the red marker on the NWs, depict the center of the NW.

Figures 17 (a-b) shows the SEM images of representative electrode pairs, corresponding to NW deposition after DEP for two minutes with an assembly bias of 1.5 V and 2 V, respectively. It was observed that the NW deposition occurs in three different configurations:

1. Deposition on the biasing electrode (left electrode): this is the most dominant deposition site for the NWs. This is in accordance with the results obtained in section 3.6 of chapter 3.

36

2. Deposition of NW bridging the biasing electrode and the floating electrode: this is the most desirable configuration for technological applications.

3. Deposition of the NWs on the floating electrode.

Figures 18 (a-c) and Figure 19 (a-c) shows the predicted NWs trajectory, NW deposition and NW sourcing volume for electrode pairs shown in Figure 17 (a-b), respectively. For the simulation, the NW orientation during DEP assembly was assumed to be the same as that of the electric field line vectors in the FEM.

As shown in Figures 17 (a-b), Figure 18 (b) and Figure 19 (b), the final deposition location and orientation of the NWs on electrodes surface are in agreement between the experimental and FEA results. However, some of the deposited NWs attached to only one of the electrode pairs displayed differences in final orientation angles. This difference between the orientation of NWs from simulation and experiment are attributed to several reasons. These reasons include local variation in electrode surface texture or edge corrugations, sliding of NWs deposited on electrode surface, and thermal gradients in the NW suspension solution that, trap NWs before DEP clamping. Nevertheless, the difference between the predicted and actual angles was still reasonable.

Additionally, besides the trajectory and final orientation, Figure 18 (b-c) and Figure 19 (b-c) also shows the farthest NW starting location for all the deposited NWs. Thus, the model is able to predict potential NW trajectories that yield localization at every experimentally observed NW deposition site.

(a)

NW starting positions and trajectories estimated by the model

(b)

NW deposition estimated by the model

(c)
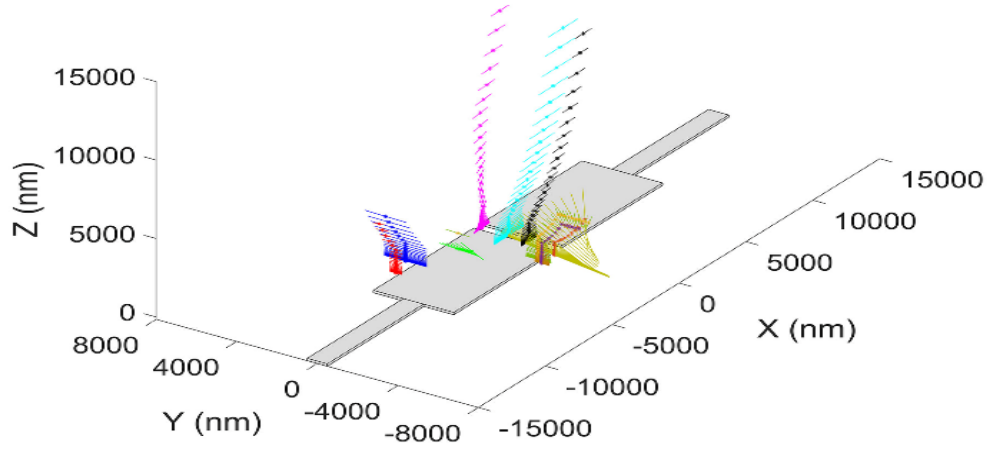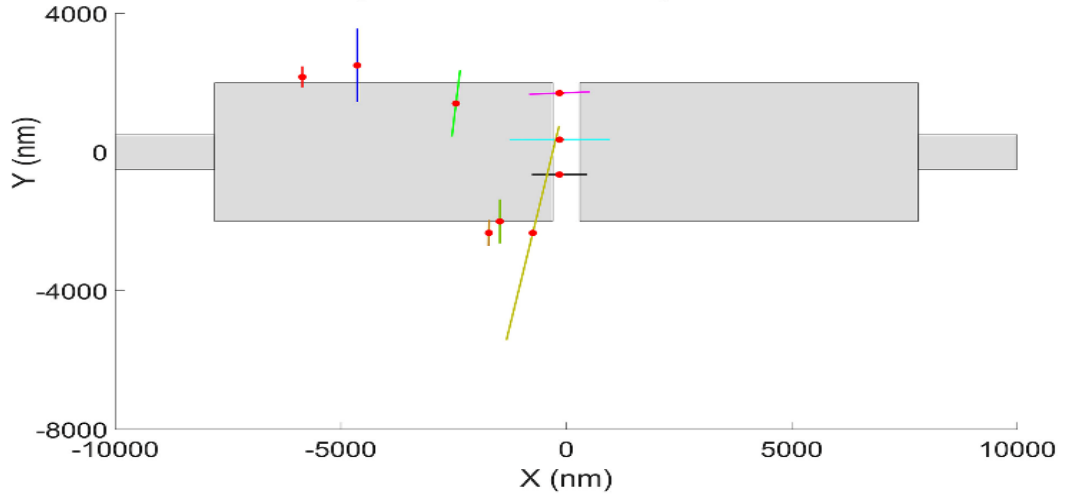
NW sourcing volume

Figure 18: (a) Predicted trajectory for each NW deposited on the electrode pair shown in Figure 17(a), (b) NW deposition and final orientation as predicted by the model. Additionally, the red dots indicate the NW center of mass (c) Sourcing volume for the farthest location of NWs deposited in Figure 17(a).

(a)

NW starting positions and trajectories estimated by the model

(b)

NW deposition estimated by the model
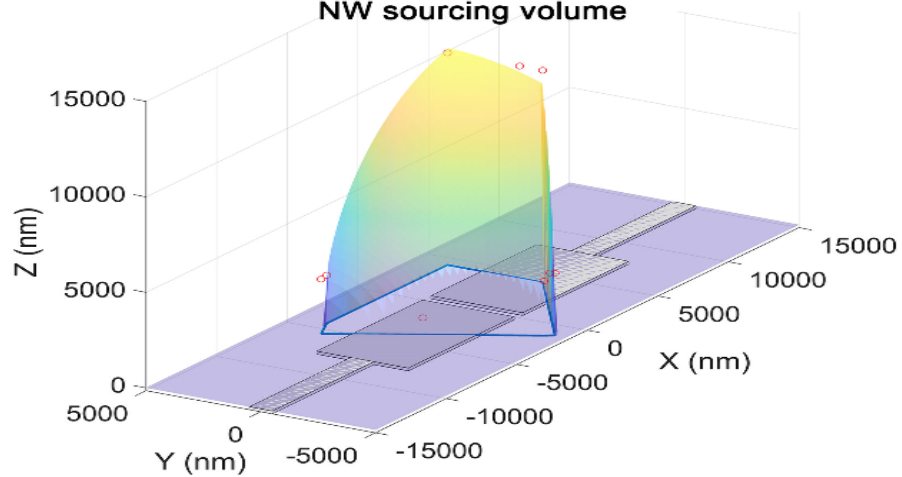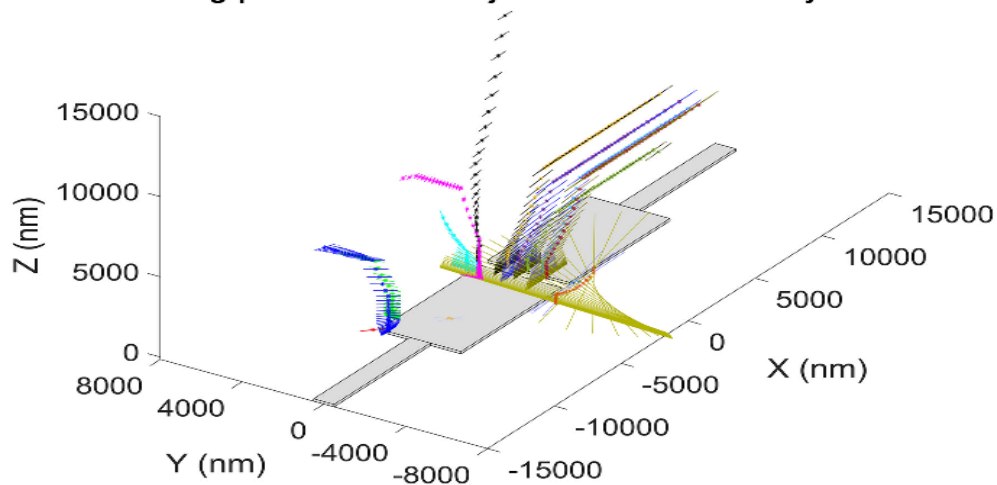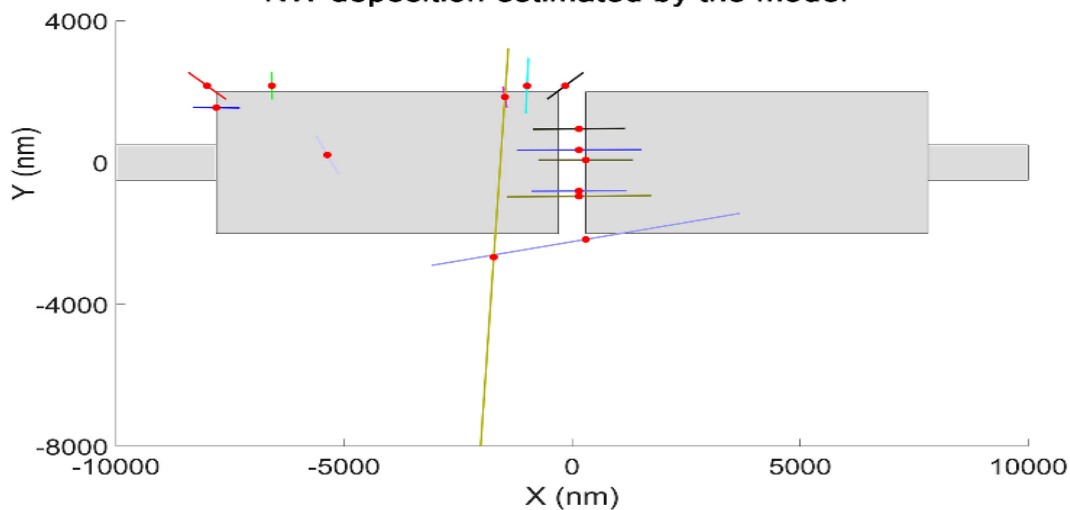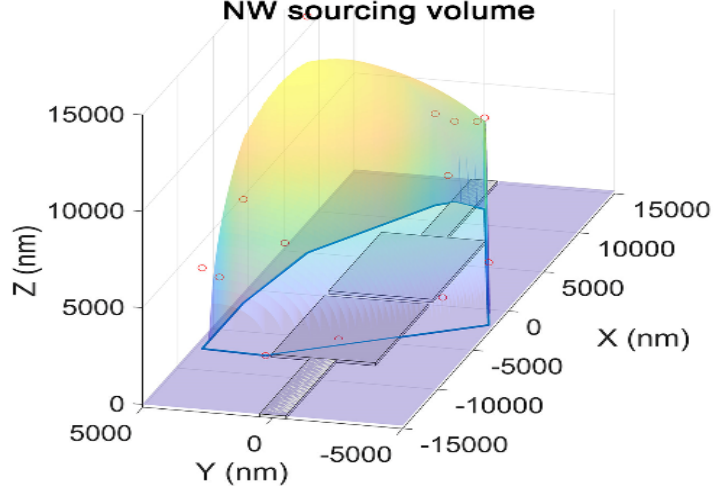

(c)

NW sourcing volume

Figure 19: (a) Predicted trajectory for each NW deposited on the electrode pair shown in Figure 17(b), (b) NW deposition and final orientation as predicted by the model. Additionally, the red dots indicate the NW center of mass (c) Sourcing volume for the farthest location of NWs deposited in Figure 17(b).

5.3.2 NW Concentration in the Colloidal Suspension

In this section, the correlation between the computational model and the experimental data is discussed. In order to verify the validity of the introduced model, the calculated NW mass concentrations are compared with the simulation results of both the experiments. This is because, the same homogenized NW suspension was simultaneously used for both the experiments. Moreover, the simulation conditions used are also similar to that of the experiments.
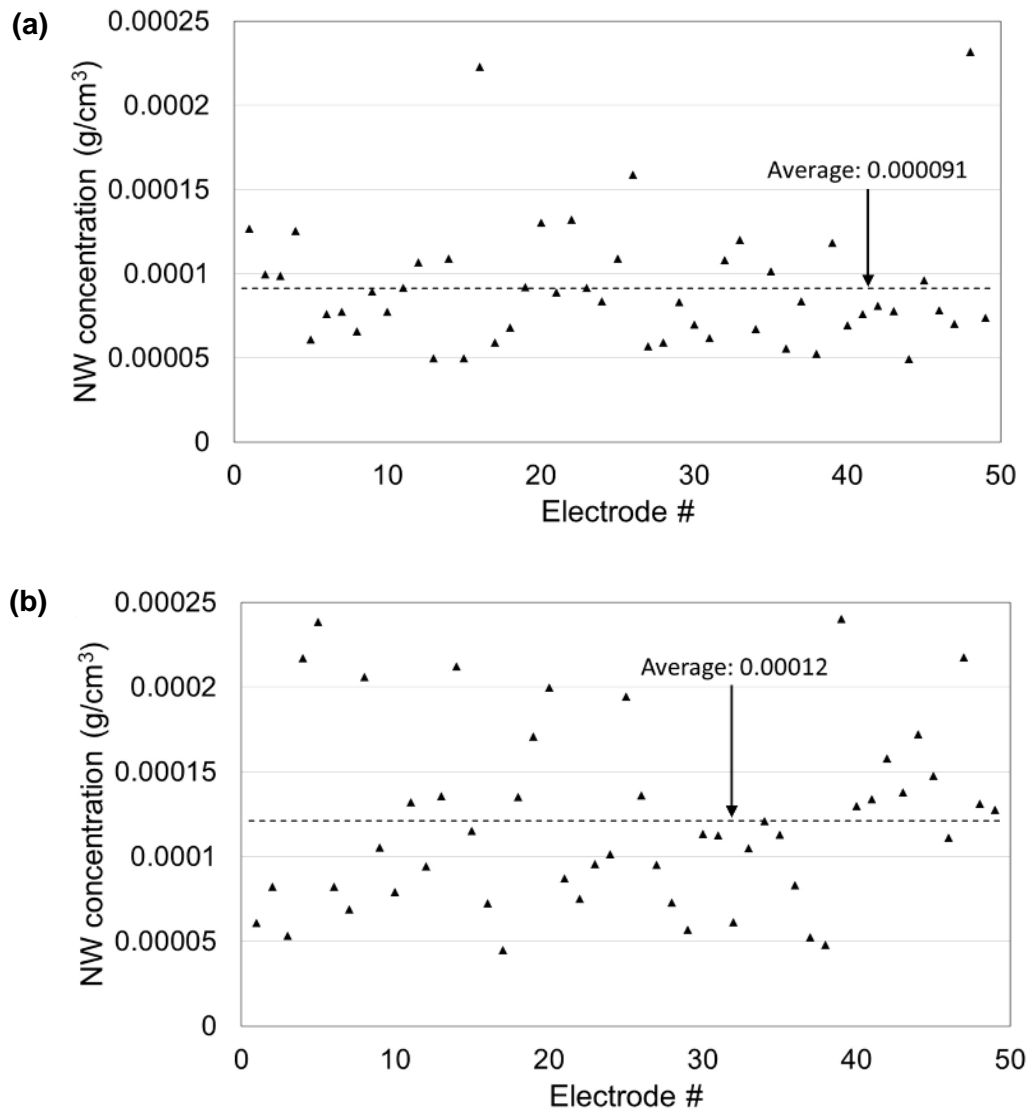

Figure 20: (a-b) Results for NW concentration (g/cc) around each electrode pair, for both experiments with bias 1.5 V and 2 V, respectively.

Therefore, comparing the mass concentration of NWs computed from models and the experiments should ideally give similar values. If the computed NW mass concentration results of both the experiments are comparable, the validity of the FEM can be established. Using the procedure mentioned in section 4.4 of chapter 4, the local NW sourcing volume (truncated volume), total mass of deposited NWs, and the NW mass concentration were determined to be 3.96×10^{-10} cc, 2.42×10^{-14} g, and 6.10×10^{-5} g/cc, respectively for the 1.5 V deposition condition (Figure 18 (a-c)). Similarly, the local NW sourcing volume, total mass of deposited NWs, and the NW mass concentration were determined to be 8.32×10^{-10} cc, 5.06×10^{-14} g, and 6.08×10^{-5} g/cc, respectively for the 2 V deposition condition (Figure 19 (a-c)). As shown, the overall mass concentration for both the cases are comparable but vary by a small amount. It is important to note that the variation in NW sourcing volume and total mass of deposited NWs vary due to localized differences in number and size (length and radius) of NWs that are obtained at each of the electrode deposition sites.

Figure 20 (a-b) depicts the NW concentration (g/cc) around each electrode pair for both experimental conditions (1.5 V and 2 V bias), which were investigated in this thesis. Note that the dotted line in the graph indicates the average NW concentration for 49 electrode pairs in both the cases. While an average concentration of 9.13×10^{-5} g/cc per electrode pair was found in the case of 1.5 V bias, an average of 12.11×10^{-5} g/cc NWs per electrode pair was found in the case of 2 V bias. Although there is a variation in computed concentration around individual electrode pairs, the difference between the average concentration was within a reasonable range (less than 32%) for the two deposition conditions. This is expected since the same sonicated NW suspension was used for both the experiments, thereby supporting the validity of computational model.

6 CONCLUSIONS

The objective of this work was to develop a 3-D electrokinetic model that calculates the imposed electric field and its resultant NW force/velocity maps within the region of influence of an electrode array operating in the FE-DEP configuration.

The following approach was implemented to achieve the objective:

1. A 3-D electrokinetic modeling framework was introduced and complementary experimental data was acquired for FE-DEP assembly of α-MnO$_2$ NWs in ethanol (chapters 2 and 3).

2. An electrokinetic model was implemented for predicting the DEP forces, nanowire trajectory, deposition location, and its farthest possible starting location within the assembly workspace (chapter 4).

3. The accuracy of the modeling approach was successfully demonstrated by comparison of the predicted NW mass concentration for all the electrode pairs involved in experiments at two different assembly conditions (chapter 5).

This comprehensive model accounts for all the relevant process parameters, which include NW size, suspension concentration, electrode design, NW starting location and deposition time. The impact of these process parameters on the resultant NW trajectory and its deposition location was also examined. The model has been validated with direct comparisons against experimental results involving FE-DEP manipulation of α-MnO$_2$ NWs. This α-MnO$_2$ NWs material system is relevant for multiple technological and next generation applications in supercapacitors, energy storage, catalysis and molecular sieves.

The approach presented will provide avenues for designing assembly platforms for ultra-high precision of any nanomaterial system. It is also expected to advance integration of FE-DEP nanoassembly-based processes with other silicon nanomachining process flows.

REFERENCES

1. A. Subramanian, N. S. Hudak, J. Y. Huang, Y. Zhan, J. Lou and J. P. Sullivan, *Nanotechnol.*, 2014, 25, 265402.

2. S. Glassner, C. Zeiner, P. Periwal, T. Baron, E. Bertagnolli and A. Lugstein, *Nano Lett.*, 2014, 14, 6699.

3. A. Kanwal, S. C. Wang, Y. Ying, R. Cohen, S. Lakshmanan, A. Patlolla, Z. Iqbal, G. A. Thomas and R. C. Farrow, *Electrochem. Commun.*, 2014, 39, 37.

4. Z. Xiao, J. Elike, A. Reynolds, R. Moten and X. Zhao, *Microelectron. Eng.*, 2016, 164, 123.

5. A. Subramanian, A. R. Alt, L. Dong, B. E. Kratochvil, C. R. Bolognesi and B. J. Nelson, *ACS Nano*, 2009, 3, 2953.

6. H. Zhao, X. Ma, J. Bai, Z. Yang, G. Sun, Z. Zhang, X. Pan, W. Lan, J. Y. Zhou and E. Xie, *Nanoscale*, 2017, 9, 8192.

7. X. Xia, J. Zhan, Y. Zhou, X. Wang, J. Tu and H. J. Fan, *Small*, 2017, 13, 1602742.

8. L. Mai, X. Tian, X. Xu, L. Chang and L. Xu, *Chemical Reviews*, 2014, 114, 11828.

9. J. Jian, X. Guo, L. Lin, Q. Cai, J. Cheng and J. Li, *Sens. Actuators, B*, 2013, 178, 279.

10. S. D. Evans, S. R. Johnson, Y. L. Cheng and T. Shen, *J. Mater. Chem.*, 2000, 10, 183.

11. B. Y. Lee, K. Heo, J. H. Bak, S. U. Cho, S. Moon, Y. D. Park and S. Hong, *Nano Lett.*, 2008, 8, 4483.

12. W. Wang, F. Lv, B. Lei, S. Wan, M. Luo and S. Guo, *Adv. Mater.*, 2016, 28, 10117.

13. D. Wang, R. Zhu, Z. Zhou and X. Ye, *Appl. Phys. Lett.,* 2007, 90, 103310.

14. P. J. Pauzauskie, A. Radenovic, E. Trepagnier, H. Shroff, P. D. Yang, and J. Liphardt, *Nat. Mater.*, 2006, 5, 97.

15. Y. Huang, X. F. Duan, Q. Q. Wei, and C. M. Lieber, *Science*, 2001, 291, 630.

16. H. J. Xin and A. T. Woolley, *Nano Lett.*, 2004, 4, 1481.

17. N. K. R. Palapati, E. Pomerantseva and A. Subramanian, *Nanoscale*, 2015, 7, 3109.

18. F. Zheng, X. Yang, Y. Wu, Z. Zhou and Z. Liu, *Carbon*, 2017, 124, 693.

19. J. Liu, M. J. Casavant, M. Cox, D. A. Walters, P. Boul, W. Lu, A. J. Rimberg, K. A. Smith, D. T. Colbert, and R. E. Smalley, *Chem. Phys. Lett.*, 1999, 303, 125.

20. P. Avouris, T. Hertel, R. Martel, T. Schmidt, H. R. Shea, and R. E. Walkup, *Appl. Surf. Sci.*, 1999, 141, 201.

21. R. Pethig, *Crit. Rev. Biotechnol.,* 1996, 60, 331.

22. G.H. Markx, Y. Huang, X.-F. Zhou and R. Pethig, *Microbiology, UK*, 1994, 140, 585.

23. V. Chaurey, C. Polanco, C. Chou and N. S. Swami, *Biomicrofluidics*, 2012, 6, 012806.

24. B. R. Burg and D. Poulikakos, *J. Mater. Res.*, 2011, 26, 1561.

25. J. J. Boote and S. D. Evans, *Nanotechnol.*, 2005, 16, 1500.

26. M. Dimaki and P. Bøggild, *Nanotechnol.*, 2004, 15, 1095.

27. M. Collet, S. Salomon, N. Y. Klein, F. Seichepine, C. Vieu, L. Nicu and G. Larrieu, *Adv. Mater.*, 2015, 27, 1268.

28. D. Xu, A. Subramanian and L. Dong, IEEE Trans. *Nanotechnol.*, 2009, 8, 449.

29. B. R. Burg, V. Bianco, J. Schneider, and D. Poulikakos, *J. Appl. Phys.*,2010, 107, 124308.

30. D. Xu, K. Shou and B. J. Nelson, *Microelectron. Eng.*, 2011, 88, 2703.

31. S. Golan, D. Elata, M. Orenstein and U. Dinna, *Electrophoresis*, 2006, 27, 4919.

32. T. Schnelle, R. Hagedorn, G. Fuhr, S. Fiedler and T. Muller, *Biochim. Biophys. Acta*, 1993, 1157, 127.

33. X.-B. Wang, Y. Huang, J.P.H. Burt, G.H. Markx and R. Pethig, *J. Phys. D: Appl. Phys.,* 1993, 26, 1278.

34. M.P. Hughes, R. Pethig, X.-B. Wang, *J. Phys. D: Appl. Phys.,* 1995, 28, 474.

35. N.G. Green, A. Ramos and H. Morgan, *J. Electrost.*, 2002, 56, 235.